PCCP

PAPER



Cite this: *Phys. Chem. Chem. Phys.*, 2024, **26**, 27763

# Experimental and theoretical study of the Sn–O bond formation between atomic tin and molecular oxygen†

Iakov A. Medvedkov, [a] Anatoliy A. Nikolayev, [b] Shane J. Goettl, [a] Zhenghai Yang, [a] Alexander M. Mebel *[c] and Ralf I. Kaiser *[a]

Received 24th September 2024,
Accepted 21st October 2024

DOI: 10.1039/d4cp03687e

rsc.li/pccp

The merging of the electronic structure calculations and crossed beam experiments expose the reaction dynamics in the tin (Sn, $^3P_j$) – molecular oxygen ($O_2$, $X^3\Sigma_g^-$) system yielding tin monoxide (SnO, $X^1\Sigma^+$) along with ground state atomic oxygen O($^3$P). The reaction can be initiated on the triplet and singlet surfaces *via* addition of tin to the oxygen atom leading to linear, bent, and/or triangular reaction intermediates. On both the triplet and singlet surfaces, formation of the tin dioxide structure is required prior to unimolecular decomposition to SnO($X^1\Sigma^+$) and O($^3$P). Intersystem crossing (ISC) plays a critical role in the reaction mechanism and extensively interosculates singlet and triplet surfaces. The studied reaction follows a mechanism parallel to that for the gas phase reaction of germanium and silicon with molecular oxygen, however, the presence of the tin atom enhances and expands ISC *via* the "heavy atom effect".

## Introduction

Since the exploitation of the main group XIV element tin (Sn) merged with the transition metal copper (Cu) in bronze alloys more than 5000 years ago,[1] the preparation and properties of subvalent tin(II) compounds together with their isovalent carbon (C), silicon (Si), and germanium (Ge) counterparts have intrigued the computational chemistry, physical inorganic, and preparative synthetic communities from the perspectives of electronic structure theory and chemical bonding.[2] From carbon to tin, the electronic structure of the dihydrides transforms noticeably. Whereas for the lightest main group XIV element carbon, the divalent hydride methylene ($CH_2$, $X^3B_1$) has a triplet electronic ground state and a singlet–triplet splitting to the a $^1A_1$ state of 36 to 38 kJ mol$^{-1}$,[3,4] all higher homologues silylene ($SiH_2$), germylene ($GeH_2$), and stannylene ($SnH_2$) hold an $X^1A_1$ electronic ground state. The singlet–triplet splitting to the a $^3B_1$ state increases from 80–88 kJ mol$^{-1}$ in silylene ($SiH_2$)[5–11] *via* 100–105 kJ mol$^{-1}$ in germylene ($GeH_2$)[12] and 98–111 kJ mol$^{-1}$ (ref. 12,13) in stannylene ($SnH_2$) as the period increases. This trend can be rationalized in terms of discrete sizes of the valence orbitals of carbon, silicon, germanium, and tin; the enhanced size of the valence orbitals of silicon, germanium, and tin compared to carbon results in an ineffective hybridization of the s and p orbitals in silicon, germanium, and tin; this is accompanied by the stabilization of the singlet *versus* triplet state in silylene, germylene, and stannylene. This finding correlates nicely with the reduction of the H–E–H angles (E = C, Si, Ge, Sn) in the electronic ground states, which are reduced from 129.8° ($CH_2$, $X^3B_1$) *via* 93.4° ($SiH_2$, $X^1A_1$) to 92.3° ($GeH_2$, $X^1A_1$) and 92.4° ($SnH_2$, $X^1A_1$).[14,15] The diminished reactivity of stannylene ($SnH_2$)[16] compared to their isovalent methylene ($CH_2$),[17–21] silylene ($SiH_2$),[22–24] and germylene ($GeH_2$) analogues[25] culminated in the preparative synthesis of subvalent tin(II) compounds such as $Sn_2[(Me_3Si)_2CH]$[26] and $Sn[N(SiMe_3)]_2$.[27]

The mounting attention in the (in)organic tin(II) chemistry and industrial applications of tin(II) oxide (SnO) in conjunction with indium tin oxide (ITO) on touchscreens and thin film transistors (TFT)[28,29] revitalized widespread research in the electronic structure and chemical bonding of binary oxides of main group XIV elements. In gas-phase carbon monoxide (CO), two π and one σ-bond generate a carbon–oxygen triple bond.[30,31] Whereas carbon monoxide is a gas at 293 K, gas-phase silicon monoxide (SiO), is unstable and disproportionates to amorphous silicon and silicon dioxide ($SiO_2$).[32,33] In the diatomic oxides, the bond lengths increase from carbon *via* silicon and germanium to tin from 112.8 pm *via* 151.2 pm and 161.7 pm to 183.3 pm.[34] The electronegativity difference

[a] *Department of Chemistry, University of Hawai'i at Manoa, Honolulu, HI 96822, USA. E-mail: ralfk@hawaii.edu*
[b] *Samara National Research University, Samara 443086, Russia*
[c] *Department of Chemistry and Biochemistry, Florida International University, Miami, Florida 33199, USA. E-mail: mebela@fiu.edu*

† Electronic supplementary information (ESI) available: Potential energy surface with included bond distances (Å) and bond angles of each transition state, intermediate, minimum on the seam of crossing. Optimized Cartesian coordinates and vibrational frequencies for all intermediates, transition states, MSX, reactants, and products involved in the reactions of the atomic tin (Sn; $^3P_j$) with oxygen ($O_2$; $X^3\Sigma_g^-$). See DOI: **https://doi.org/10.1039/d4cp03687e**

between the main group XIV element and oxygen rises from 1.00 in carbon monoxide (CO) to 1.78 in tin monoxide (SnO) on the Pauling scale suggesting an enhanced ionic character in the tin–oxygen bond compared to the carbon–oxygen bond. Also, within main group XIV, the +II oxidation state becomes increasingly stable as demonstrated by the stability of commercially available tin(II) and tin(IV) compounds such as tin(II) chloride and tin(IV) sulfide. Nevertheless, tin(IV) is still considered to be more stable than tin(II); as such, tin monoxide (SnO) emerged as a reduction agent that can be oxidized easily to tin dioxide ($SnO_2$).[35] Chlorides and organic compounds such as tin tetrachloride ($SnCl_4$), tetramethyltin ($(CH_3)_4Sn$), and dimethyldichlorotin ($(CH_3)_2SnCl_2$) are used as precursors for the gas-phase synthesis of tin dioxide. These precursors decompose[36–38] into atomic tin, which also makes studying the reaction of tin plus molecular oxygen ($O_2$) an indispensable step to untangle the reaction mechanism during the synthesis of tin dioxide. Previously, the kinetics of the reaction of atomic tin with molecular oxygen was studied at high temperatures of 1300 to 2600 K using a shock tube equipped for atomic resonance absorption spectroscopy (ARAS),[39,40] in a fast-flow reactor with laser-induced fluorescence (LIF) over the wide temperature range 380 to 1840 K.,[41] and by flash photolysis absorption spectroscopy at 295 K.[42–44] Studies demonstrate that the reaction is spin-allowed and the main products are tin monoxide (SnO, $X^1\Sigma^+$) and atomic $O(^3P)$. Rate constants measurements show that the reaction is relatively fast, with a slight positive temperature dependence (Table 1). It must be mentioned that in 1978,[45] the reaction of atomic tin with molecular oxygen was tried in a crossed molecular beam setup with a high-temperature (1525 K) molten source for the tin beam. However, the authors were unable to experimentally verify the reaction energy, and the level of development of quantum chemical calculations at the moment would not have allowed them to elucidate the reaction mechanism of such an electron-rich system.

However, whereas tin dioxide ($SnO_2$) has been successfully synthesized in the gas phase exploiting flame spray pyrolysis and droplet combustion techniques,[46] no route has been developed to prepare divalent tin monoxide (SnO) in a directed synthesis. Here, we report the gas-phase preparation of tin monoxide (SnO, $X^1\Sigma^+$) through the bimolecular reaction of ground state tin atoms (Sn; $^3P_j$) with molecular oxygen ($O_2$; $X^3\Sigma_g^-$) utilizing the crossed molecular beams technique.[47,48] An elucidation of elementary reactions at the microscopic level in tandem with electronic structure calculations affords remarkable insights into the intimate reaction dynamics through which highly reactive subvalent oxides like tin oxide (SnO, $X^1\Sigma^+$) can be generated *via* a single collision event between atomic tin and a prototype oxidant ($O_2$; $X^3\Sigma_g^-$) under single-collision conditions in the gas phase through non-adiabatic reaction dynamics. This reaction is also of fundamental importance to the reaction dynamics community as a benchmark of triatomic systems involving the 'heavy' main group XIV element tin, which has been elusive until now, and the comparison with the isovalent Si–$O_2$[49] and Ge–$O_2$[50] systems explored previously.

## Experimental and computational

### Experimental

The gas-phase reaction of atomic tin (Sn, $^3P_j$) with molecular oxygen ($O_2$, $X^3\Sigma_g^-$) was carried out under single-collision conditions using the crossed molecular beams machine.[47,51] The experimental setup, data acquisition, and data processing are described elsewhere in detail.[47–49] Briefly, the reactant atomic tin (Sn, $^3P_j$) was generated *in situ* in the primary source chamber by laser ablation (3 mJ, 266 nm, 30 Hz; Quanta-Ray) from a rotating tin rod (99.98% Sn, Alfa Aesar) and seeding the ablated atoms in a pulsed argon beam (Ar, 99.9999%; Airgas) that was released from a piezoelectric valve operating at 60 Hz and a backing pressure of 4 atm (Fig. 1a). All five most abundant isotopes of tin[52] were detected in the beam with the signal ratios matching their natural abundance (Table 2). The atomic tin beam was skimmed and velocity selected using a four-slot chopper wheel; this achieved a peak velocity $v_p = 631 \pm 22$ m s$^{-1}$ and speed ratio $S = 8.5 \pm 0.6$. Neat oxygen gas (550 Torr, $O_2$, 99.998%; Matheson) was used as a precursor to produce the 'reactant two' supersonic molecular oxygen beam (60 Hz, $v_p = 776 \pm 20$ m s$^{-1}$, $S = 15.6 \pm 1.0$) in the secondary source chamber. Both molecular beams intersected at an angle of 90° in the scattering chamber at a mean collision energy of $E_C = 13 \pm 1$ kJ mol$^{-1}$. The reactively scattered products were ionized by electron ionization at 80 eV (2 mA) at the entrance of the rotatable detector, filtered according to $m/z$ by the QMS (Extrel, QC 150; 1.2 MHz), and detected using a Daly-type particle ion counter (Fig. S1, ESI†).[53] Angularly resolved time-of-flight (TOF) spectra were recorded at discrete laboratory angles in 2.5° steps (Fig. 1b). Operating the laser at half frequency of the pulsed valves and sufficient length of the recorded TOFs allowed an

Table 1 Experimentally measured rate constants for reaction of Sn($^3P_j$) with $O_2$

| Method[a] | $k$, cm$^3$ molecule$^{-1}$ s$^{-1}$ | Temperature range, K | Source |
|---|---|---|---|
| Shok tube, ARAS | $10^{-9.80} \times e^{-11.7\ \mathrm{kJ\ mol^{-1}}/RT}$ | 1350–2600 | Ref. 39 |
| | $10^{-9.41 \pm 0.03} \times e^{-11.5 \pm 1.1\ \mathrm{kJ\ mol^{-1}}/RT}$ | 1300–2250 | Ref. 40 |
| Fast-flow reactor, LIF | $10^{-12.29}\ (T/\mathrm{K})^{0.79} \times e^{-3.6\ \mathrm{kJ\ mol^{-1}}/RT}$ | 380–1840 | Ref. 41 |
| Flash photolysis absorption | $1.05 \pm 0.08 \times 10^{-11}$ | 295 | Ref. 42 |
| | Sn($^3P_0$): $2.1 \pm 0.1 \times 10^{-11}$ | | Ref. 43 |
| | Sn($^3P_0$): $3.5 \pm 0.4 \times 10^{-11}$ | | Ref. 44 |
| | Sn($^3P_1$): $8.2 \pm 0.5 \times 10^{-11}$ | | |
| | Sn($^3P_2$): $4.91 \pm 0.3 \times 10^{-11}$ | | |

[a] ARAS – atomic resonance absorption spectroscopy, LIF – laser-induced fluorescence.

 

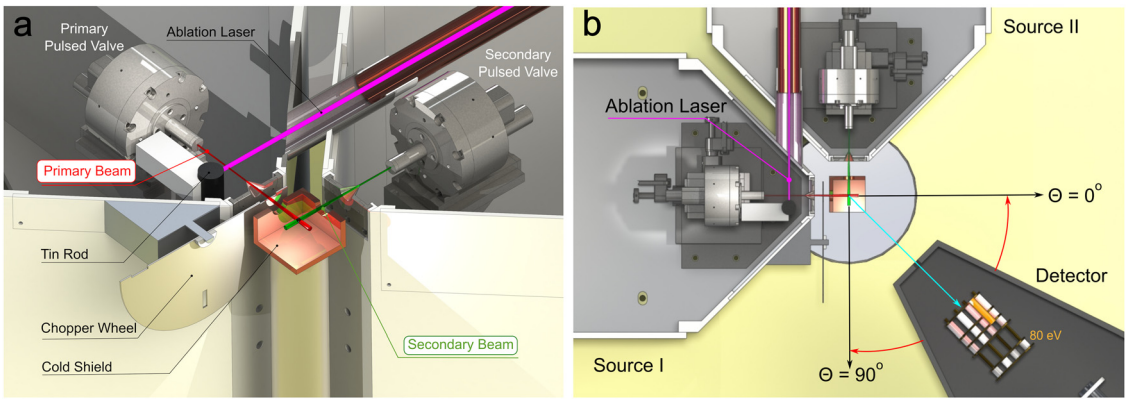


Fig. 1 Experimental setup. (a) Side view on the cross point; (b) Top-view of the experiment with the detector.

Table 2 Theoretical and experimental ratios of signal for different tin isotopes in the received atomic tin beam in argon

| | $^{120}$Sn | $^{119}$Sn | $^{118}$Sn | $^{117}$Sn | $^{116}$Sn |
|---|---|---|---|---|---|
| Abundance | 32.6% | 8.6% | 24.2% | 7.7% | 14.5% |
| Theoretical ratio of signal[a] | 1 | 0.26 | 0.75 | 0.24 | 0.44 |
| Experimental ratio in beam | 1 | 0.25 ± 0.01 | 0.74 ± 0.01 | 0.24 ± 0.01 | 0.49 ± 0.01 |

[a] Ratio to the most abundant isotope $^{120}$Sn.

instant background subtraction ("laser-on" minus "laser-off") during the TOF recording.

To gain information on the reaction dynamics, TOF spectra and the laboratory angular distribution (LAD) were transformed from the laboratory to the center-of-mass frame by a forward-convolution routine.[54,55] This approach uses initially a trial angular flux $T(\theta)$ and translational energy $P(E_T)$ distributions in the center-of-mass (CM) frame to simulate the TOFs and LAD (laboratory data). CM functions were iteratively varied until the best fit of the TOF spectra and LAD was achieved. Together the CM functions constitute the reactive differential cross sections $I(\theta, u) \sim P(u) \times T(\theta)$, where $u$ – the CM velocity, $\theta$ – angle in the CM system. The reactive differential cross sections can be represented as a flux contour map that depicts the probability of the products to scatter at the specific angle ($\theta$) with the specific kinetic energy ($u$).

## Computational

Being a heavy atom with 50 electrons, tin requires consideration of relativistic effects by using a relativistic effective core potential (ECP).[56–58] 28 electrons at the $1s^2 2s^2 2p^6 3s^2 3p^6 3d^{10}$ set of orbitals of Sn are described by means of Stuttgart ECP28MDF[57] and therefore, the number of electrons on the tin atom explicitly included in the computations is 22 at the $4s^2 4p^6 5s^2 4d^{10} 5p^2$ set of orbitals, making the total number of electrons for the $SnO_2$ system to be 38. The hybrid ωB97X-D density functional theory[59] with Dunning's augmented correlation-consistent triple-ζ basis sets aug-cc-pVTZ (for O) and aug-cc-pVTZ-PP (for Sn)[56,57,60] in the Gaussian 09 software package[61] was originally applied to optimize geometries and to compute vibrational frequencies of the intermediates and transition states on the $SnO_2$ potential energy surface (PES). All the structures were subsequently reoptimized in Molpro 2015[62] utilizing the multireference second-order perturbation theory (CASPT2) method[63,64] with the augmented quadruple-ζ basis sets aug-cc-pVQZ (for O) and aug-cc-pVQZ-PP (for Sn)[56,57,60] and with full valence active space containing 16 electrons distributed on 12 orbitals ($5s^2 5p^2$ for tin and two sets of $2s^2 2p^4$ for oxygen). The CASPT2 wavefunctions used initial orbitals taken from full valence, multireference complete active space self-consistent field (CASSCF) calculations[65,66] with the same quadruple-ζ basis sets.[56,57,60] All calculations were carried out within the $C_s$ point group, with the numbers of orbitals included in the active space ('occupied') and those kept closed being 17A′ + 6A″ and 8A′ + 3A″, respectively, thus resulting in 12 active orbitals (9A′ + 3A″). It should be noted that in the CASPT2 calculations $4s^2 4p^6$ electrons of tin and $1s^2$ of each oxygen were treated as a core (5A′ + 1A″) and not included in single and double excitations, with only $4d^{10}$ (3A′ + 2A″) electrons of Sn involved beyond the active space. Thus, 26 electrons of $SnO_2$ participated in the dynamic electronic correlation calculations.

The minimal energy structures on the seams of crossing (MSX) between singlet ($^1$A′) and triplet ($^3$A′ or $^3$A″) states and between two different triplet states ($1^3$A′–$2^3$A′ or $^3$A′–$^3$A″) were located using Molpro 2015 using two alternative approaches. First, the CASSCF(16,12) method with the Karlsruhe segmented contracted, split-valence triple-ζ def2-TZVPPD basis set containing two sets of polarization functions and a set of diffuse function[67,68] was employed for the conical intersection optimization followed by CASPT2(16,12)/aug-cc-pVQZ-(PP) single-point calculations for the MSX energy refinement. Where the direct MSX optimization was unsuccessful, we utilized CASSCF(16,12)/aug-cc-pVQZ-(PP) (PP relates only to Sn) and CASPT2(16,12)/aug-cc-pVQZ-(PP) single-point computations to carry out two-dimensional potential

energy scans separately for each state in relevant regions of the PES. Such regions were identified based on the constructed potential energy diagram for the electronic states involved.

Furthermore, the energies of the reactants and products were calculated both at the coupled clusters[69] CCSD(T)/CBS//ωB97X-D/aug-cc-pVTZ-(PP) level with the complete basis set (CBS) extrapolation from the values obtained with the aug-cc-pVQZ-(PP) and aug-cc-pVTZ-(PP) basis sets for isolated Sn, $O_2$, SnO, and O and at the CASPT2(16,12)/aug-cc-pVQZ-(PP)/ωB97X-D/aug-cc-pVTZ-(PP) level considering the reactants Sn + $O_2$ and the products SnO + O as supermolecules, with two fragments positioned sufficiently far from one another so that their interaction is negligible. The two theoretical methods used have resulted in practically the same reaction energy. Finally, potential energy scans at the CASPT2(16,12)/aug-cc-pVQZ-(PP) level of theory were implemented to explore the entrance $O_2$ addition channel for the formation of an initial triplet intermediate and the exit O elimination channel on the triplet PES and to verify barrierless connections between the $SnO_2$ intermediates with reactants/products.

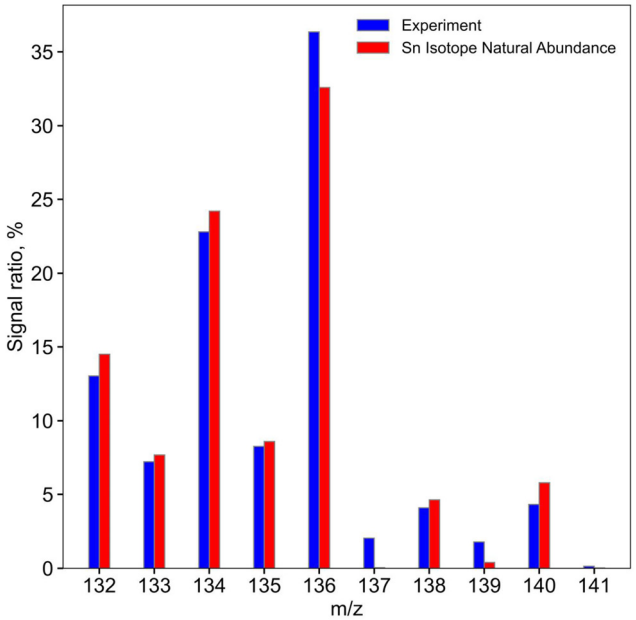


Fig. 2 The ratio of the signal for the reaction of atomic tin with molecular oxygen at the center-of-mass angle at different $m/z$. The blue bars are the experimental results, red – predicted ratio according to the natural isotope abundance of tin.

## Results and discussion

### Laboratory frame

The ratios of the natural isotope abundances of tin $^{116}$Sn, $^{117}$Sn, $^{118}$Sn, $^{119}$Sn, $^{120}$Sn, $^{122}$Sn, and $^{124}$Sn are 14.5, 7.7, 24.2, 8.6, 32.6, 4.6 and 5.8%, respectively. Therefore, the reactive scattering signal for tin monoxide (SnO) was initially monitored in the range of $m/z$ 132–141. The ratio of the collected signal of tin monoxide at the center-of-mass angle nicely matches the prediction from the natural abundance of tin isotopes (Fig. 2). Non-zero signals at $m/z$ = 137 and 139 arise from the presence of $^{18}$O isotopes.

These raw data alone demonstrate a single reaction channel *via* the emission of atomic oxygen (16 amu) and formation of tin monoxide ($^{116}Sn^{16}O^+$, $m/z$ = 132; $^{117}Sn^{16}O^+$, $m/z$ = 133; $^{118}Sn^{16}O^+$, $m/z$ = 134; $^{119}Sn^{16}O^+$, $m/z$ = 135; $^{120}Sn^{16}O^+$, $m/z$ = 136; $^{122}Sn^{16}O^+$, $m/z$ = 138; $^{124}Sn^{16}O^+$, $m/z$ = 140) in the reaction of atomic tin with molecular oxygen. The corresponding TOF spectra were collected at the best signal-to-noise ratio at $m/z$ = 136 (Fig. 3) and were then normalized to the signal at the CM angle to obtain the laboratory angular distribution (LAD). More than $2.5 \times 10^6$ TOF spectra were recorded between $8.75^\circ \leq \Theta \leq 58.75^\circ$ with the tin beam defined as $\Theta = 0^\circ$ direction. The LAD is rather wide, starts at 53.75°, and extends beyond the range of the rotating detector at small angles (less than 8.75°). The TOF spectra are broad from at least 700 to 1500 μs and peak between 750 and 900 μs. These findings propose that the tin monoxide products were formed *via* indirect scattering dynamics through complex formation involving $SnO_2$ intermediates.[47,70,71]

### Center-of-mass frame

To further illuminate the underlying reaction mechanism(s) accompanied by the potential involvement of intersystem crossing (ISC), excited state surfaces, and non-adiabatic reaction dynamics, a transformation of the laboratory data from the laboratory reference frame into the center-of-mass reference frame is accomplished using a single channel fit of the laboratory data and reaction (1):

$$^{120}Sn(^3P_j) + {}^{16}O_2(X^3\Sigma_g^-) \rightarrow {}^{120}Sn^{16}O(X^1\Sigma^+) + {}^{16}O(^3P). \quad (1)$$

The best-fit CM functions are depicted in Fig. 4a and b. The error ranges of the $P(E_T)$ and $T(\theta)$ functions are determined within the 1$\sigma$ limits of the corresponding laboratory angular distribution and beam parameters (beam spreads and beam velocities) while maintaining a good fit of the laboratory TOF spectra and LAD. The translational energy flux distribution $P(E_T)$ (Fig. 4a) contains valuable information about reaction dynamics and thermodynamics. The derived $P(E_T)$ distributions exhibit a maximum translational energy release ($E_{max}$) of 76 ± 12 kJ mol$^{-1}$. Energy conservation dictates that for those molecules born without internal excitation, $E_{max}$ is the sum of the collision energy ($E_C$) and the reaction energy. Taking into account the collision energy of 13 ± 1 kJ mol$^{-1}$, the reaction energy was determined to be exoergic by 63 ± 13 kJ mol$^{-1}$. Thermodynamic analysis of our experimental results proves the observation of reaction (1) with stated electronic and spin–orbit levels. In the case of the presence of only the Sn($^3P_0$) in the beam reaction energy would be −24 kJ mol$^{-1}$, while reaction energy calculated for the Sn($^3P_2$) provides a close match (−65 kJ mol$^{-1}$) with the experimental data. Sn($^3P_0$) and Sn($^3P_1$) are also present in the beam but masked in the lower energy section of the CM translational energy distribution (Fig. 4a). Production of higher energetic species SnO($a^3\Sigma^+$) or O($^1D$) drives the reaction endoergic to +208[72] or +166 kJ mol$^{-1}$, respectively. These reactions are closed under our experimental

 

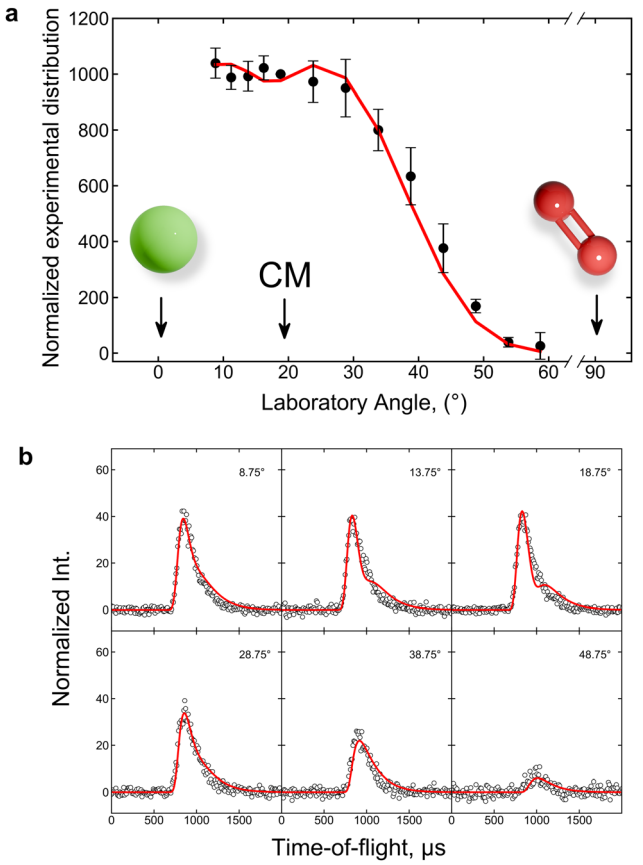


Fig. 3 (a) Laboratory angular distribution (b) and time-of-flight (TOF) spectra recorded at $m/z$ = 136 for the reaction of the tin atom with molecular oxygen at a collision energy of 13 ± 1 kJ mol$^{-1}$. The circles represent the experimental data and the solid lines are the best fits, the green atom is tin, red atoms are oxygen.

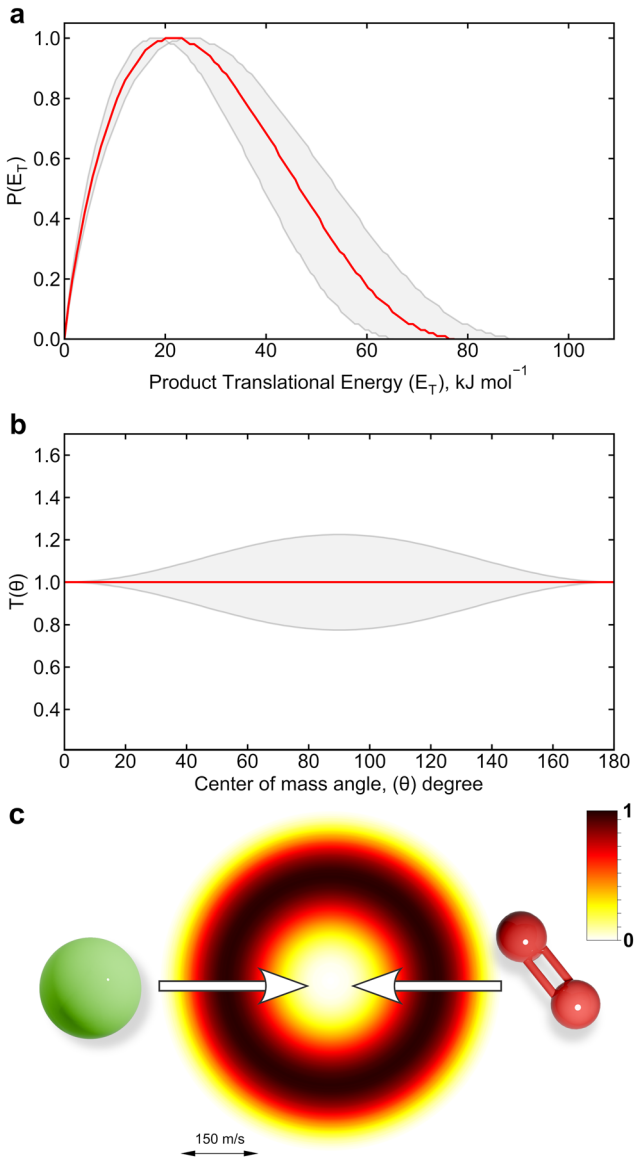


Fig. 4 (a) Center-of-mass translational energy $P(E_T)$, (b) angular $T(\theta)$ flux distributions, and (c) flux contour map for the reaction of the tin atoms with molecular oxygen. The solid lines represent the best fit, while the shaded areas indicate the error limits. For $T(\theta)$, the direction of the tin beam is defined as 0° and of the oxygen as 180°. The green atom is tin, red atoms are oxygen.

conditions with $E_C$ = 13 ± 1 kJ mol$^{-1}$. The average translational energy of the products was derived to be 28 ± 5 kJ mol$^{-1}$, suggesting that 38 ± 12% of the total available energy is channeled into the translational degrees of freedom of the products, which usually implies that the reaction mechanism proceeds through the formation of a covalently bound intermediate.[47,70,71] The center-of-mass angular distribution $T(\theta)$ can provide additional information about the reaction dynamics (Fig. 4b). The 'flat' $T(\theta)$ reveals that products after a collision are scattered in all directions with equal probability (isotropic scattering). The forward-backward symmetry and intensity distribution also propose indirect scattering dynamics *via* long-lived (longer than their rotational periods) $SnO_2$ complex(es).[73] Foresaid findings are also enclosed in the flux contour map (Fig. 4c), which depicts an overall image of the reaction scattering process.

### Reaction mechanism

Now we combine our experimental results with electronic structure calculations to unlock the underlying chemical dynamics and reaction mechanism(s) of atomic tin oxidation in the gas phase. For the $Sn(^3P_j) + O_2(X^3\Sigma_g^-)$ reaction, both reactants are in their triplet electronic ground states; since the accessible products are tin monoxide (SnO, $X^1\Sigma^+$) and atomic oxygen $O(^1D/^3P)$, close scrutiny has to be attributed to the triplet and singlet $SnO_2$ surfaces. Here, the computations identified three singlet (**i1**, **i4**, and **i8**) and five triplet (**i2**, **i3**, **i5**, **i6**, **i7**) $SnO_2$ intermediates, six transition states (**ts1–ts6**), five singlet–triplet seams of crossings (**MSX1a**, **MSX1b**, **MSX2**, **MSX7**, and **MSX8**), and eight triplet–triplet seams of crossings (**MSX3–MSX6**, **MSX9–MSX12**).

The singlet surface (Fig. 5, red) can be accessed *via* two barrierless entrance channels: end-on addition with the formation of a linear (SnOO, **i4**, $C_{\infty v}$, $^1\Sigma^+$) or side-on addition leading to a triangular ($SnO_2$, **i1**, $C_{2v}$, $^1A_1$) intermediate. The triangular intermediate **i1** can undergo either Sn–O bond

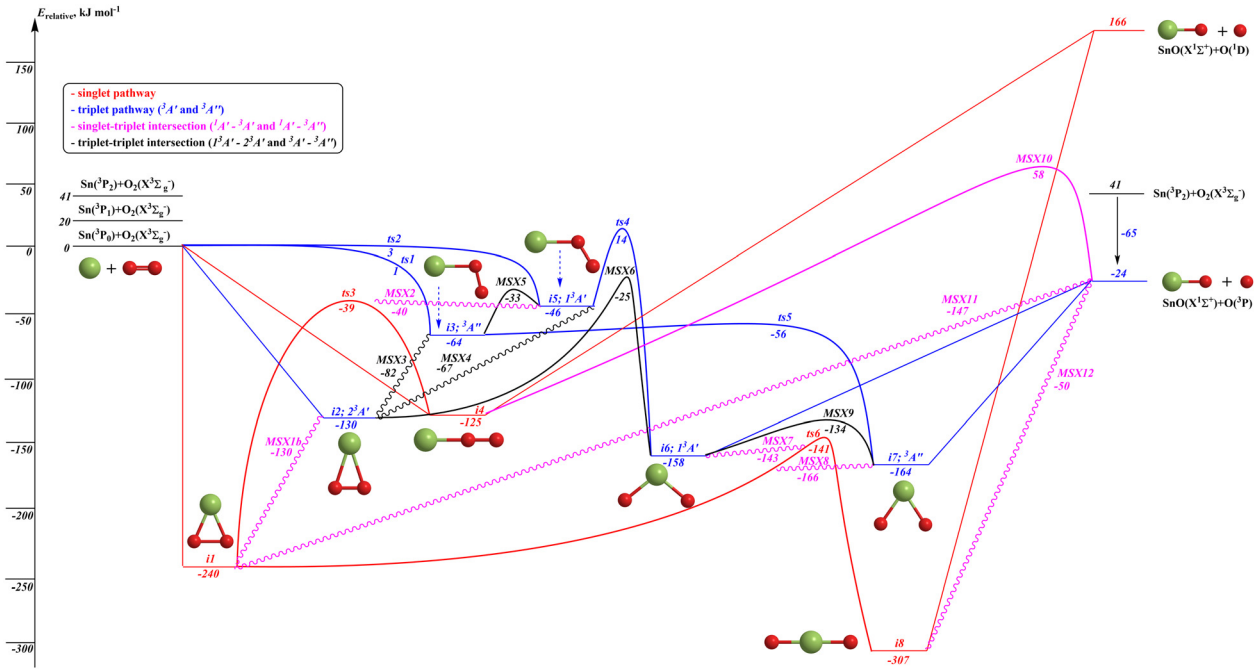


Fig. 5 Potential energy surface (PES) of the reaction of atomic tin (Sn, $^3P_j$) with oxygen ($O_2$, $X^3\Sigma_g^-$). The italic numbers colored red, blue, black, and pink give the energies at the CASPT2(16,12)/aug-cc-pVQZ-(PP) (PP relates to Sn) level of theory with ZPE at the ωB97X-D/aug-cc-pVTZ-(PP) level of theory. The reaction energies of the products are calculated using CCSD(T)/CBS(aug-cc-pV(T+Q)Z-(PP))//ωB97X-D/aug-cc-pVTZ-(PP). The geometries of MSXs are either optimized at the CASSCF(16,12)/def2-TZVPPD level of theory, with their single-point energies recalculated at the CASPT2(16,12)/aug-cc-pVQZ-(PP) level of theory, or located using two-dimensional scans of the PES at the CASPT2(16,12)/aug-cc-pVQZ-(PP) level of theory. The energies are shown in kJ mol$^{-1}$. The tin atoms are colored green, and the oxygen atoms are colored red. Detailed structural parameters of the intermediates, transition states, and MSX are given in Fig. S2 in ESI.†

rupture to **i4** *via* a high barrier of 201 kJ mol$^{-1}$ or O–O bond cleavage *via* a 99 kJ mol$^{-1}$ barrier to the linear tin dioxide structure **i8** (OSnO, $D_{\infty h}$, $^1\Sigma_g^+$). Both **i4** and **i8** have an only spin-allowed exit channel without a transition state to tin monoxide SnO($X^1\Sigma^+$) plus O($^1$D) with a total reaction endothermicity of 125–166 kJ mol$^{-1}$ (depending on the initial state of the Sn atom). On the triplet surface (Fig. 5, blue), the reaction can be initiated *via* the addition of ground-state tin to one of the oxygen atoms of molecular oxygen leading to the bent triplet intermediates **i3** (∠SnOO = 103°, $C_s$, $^3A''$) or **i5** (∠SnOO = 121°, $C_s$, $^3A'$) *via* tiny barriers of 1 or 3 kJ mol$^{-1}$, respectively. Intermediates **i5** and **i3** can isomerize *via* migration of the terminal oxygen atom to the tin atom accessing bent tin dioxide structures **i6** (∠OSnO = 101°, $C_{2v}$, $^3B_2$) and **i7** (∠OSnO = 68°, $C_{2v}$, $^3B_2$), respectively. Both **i6** and **i7** undergo a barrierless, unimolecular decomposition to tin monoxide (SnO, $C_{\infty v}$, $X^1\Sigma^+$) and ground state atomic oxygen (O($^3$P)).

Both ISC take place at the energies lower than that of the products making these exit channels practically barrierless in the reverse direction. Interestingly, the bent **MSX11** structure occurs early on the decomposition pathway of **i1** lying 123 kJ mol$^{-1}$ below the products, with the breaking Sn–O bond lengthened to 2.140 Å. Alternatively, the linear **MSX12** structure is late, only 26 kJ mol$^{-1}$ lower than the products and with breaking a Sn–O bond of 2.430 Å. The other exit **MSX10** on the pathway from **i4** to the SnO($X^1\Sigma^+$) + O($^3$P) products resides 82 kJ mol$^{-1}$ above the products making this channel non-competitive. Singlet–triplet crossings also connect **i1** with **i2** (**MSX1a** (in SI) and **MSX1b** occurring in the close vicinity of **i2**), **i1**/**i4** with **i5** (**MSX2** in the vicinity of singlet **ts3**), and **i8** with **i6** and **i1** with **i7** (**MSX7** and **MSX8**, respectively, both located in the vicinity of singlet **ts6**). The other MSXs are responsible for internal conversion (IC) processes between different triplet PESs. For instance, **MSX3** and **MSX4** lead from **i2** to **i3** and **i5**, respectively, and reside lower in energy than **i3** and **i5**. **MSX5**, **MSX6**, and **MSX9** play the role of barriers for the interconversion of **i3** to **i5**, **i2** to **i6**, and **i6** to **i7**, respectively.

Considering the energetics of the transition states, MSXs, and products, we can conclude that the most favorable reaction pathways include spin-allowed and adiabatic Sn($^3P_j$) + O$_2$($X^3\Sigma_g^-$) → **ts1** → **i3** → **ts5** → **i7** → SnO($X^1\Sigma^+$) + O($^3$P), spin-allowed non-adiabatic Sn($^3P_j$) + O$_2$($X^3\Sigma_g^-$) → **i1** → **MSX1b** → **i2** → **MSX3** → **i3** → **ts5** → **i7** → SnO($X^1\Sigma^+$) + O($^3$P), Sn($^3P_j$) + O$_2$($X^3\Sigma_g^-$) → **ts2** → **i5** → **MSX5** → **i3** → **ts5** → **i7** → SnO($X^1\Sigma^+$) + O($^3$P), Sn($^3P_j$) + O$_2$($X^3\Sigma_g^-$) → **i1** → **ts6** → **MSX8** → **i7** → SnO($X^1\Sigma^+$) + O($^3$P), and Sn($^3P_j$) + O$_2$($X^3\Sigma_g^-$) → **i1** → **ts6** → **MSX7** → **i6** → SnO($X^1\Sigma^+$) + O($^3$P), and spin-forbidden non-adiabatic Sn($^3P_j$) + O$_2$($X^3\Sigma_g^-$) → **i1** → **MSX11** → SnO($X^1\Sigma^+$) + O($^3$P) and Sn($^3P_j$) + O$_2$($X^3\Sigma_g^-$) → **i1** → **ts6** → **i8** → **MSX12** → SnO($X^1\Sigma^+$) + O($^3$P). The competition between these channels can only be theoretically evaluated through cost-forbidden non-adiabatic *ab initio* molecular dynamics simulations involving multiple triplet and singlet PESs.

 

## Conclusions

In conclusion, a merging of the electronic structure calculations and crossed beam experiments exposes the reaction dynamics in the tin (Sn, $^3P_j$) – molecular oxygen ($O_2$, $X^3\Sigma_g^-$) system forming tin monoxide (SnO, $X^1\Sigma^+$) along with atomic oxygen O($^3$P) in its electronic ground state. The reaction can be initiated on the singlet or triplet surfaces *via* additions of tin to the oxygen atom leading to linear, bent, or triangular structures. On both surfaces formation of a tin dioxide structure is required prior to unimolecular decomposition to SnO($X^1\Sigma^+$) and O($^3$P) on the triplet surface and SnO($X^1\Sigma^+$) with O($^1$D) on singlet PES. ISC and IC play important roles in this system and extensively interosculate the singlet and triplet surfaces *via* singlet–triplet (Fig. 5) and triplet–triplet (Fig. 5) intersections, respectively, *via* 13 minima on the seams of crossings (MSX). Thus, the starting channel on the triplet surface that leads to the barrier-free formation of triangular intermediate **i2** ($SnO_2$, $C_{2v}$, $^1A_1$) will be a cul-de-sac pathway in case of the absence of IC. What is interesting, a more thermodynamically competitive singlet surface without ISC channels has exit channels only to thermodynamically unfavorable SnO($X^1\Sigma^+$) and O($^1$D), which is not feasible under our collision energy of 13 kJ mol$^{-1}$. However, ISC offers direct barrier-free exit channels to SnO($X^1\Sigma^+$) and O($^3$P) products from **i1** and **i8** and the influence of the singlet surface on our experimental results cannot be excluded. The ISC is likely supported by the ''heavy atom effect'' of tin because the inclusion of heavy atoms in the molecular structure enhances the spin–orbit coupling between singlet and triplet states.[74–77] In general, studied reactions of atomic oxidation for elements from XIV group (E = Si, Ge, Sn):[49,50]

$$E(^3P_j) + O_2(X^3\Sigma_g^-) \rightarrow EO(X^1\Sigma^+) + O(^3P/^1D); \qquad (2)$$

follows a similar mechanism, with a singlet surface having exit channels only to EO($X^1\Sigma^+$) + O($^1$D) and triplet to EO($X^1\Sigma^+$) + O($^3$P) without ISC. Within the Si → Ge → Sn series with increasing atomic radius: (i) enthalpy of reaction channels to EO($X^1\Sigma^+$) + O($^1$D) and to EO($X^1\Sigma^+$) + O($^3$P) increases with equal steps around ∼140 kJ mol$^{-1}$ for each channel: −303 → −170 → −24 kJ mol$^{-1}$ and −107 → +20 → +166 kJ mol$^{-1}$, respectively; (ii) ISC effects enhances and expands.

## Author contributions

Supervision and Funding acquisition – R. I. K., A. M. M; formal analysis – I. A. M.; investigation – I. A. M., Z. Y. and S. J. G. carried out the experimental measurements, A. A. N. – carried out the theoretical analysis; Writing original draft – I. A. M.; writing – review & editing – R. I. K., A. M. M., A. A. N., I. A. M.

## Data availability

Essential data are provided in the main text and the ESI.† Raw data for crossed molecular beams experiment is available at https://doi.org/10.5281/zenodo.13831697.

## Conflicts of interest

There are no conflicts to declare.

## Acknowledgements

This work at the University of Hawaii was supported by the U.S. National Science Foundation (CHE 2244717).

## Notes and references

1 M. E. Weeks, The discovery of the elements. I. Elements known to the ancient world, *J. Chem. Educ.*, 1932, **9**, 4.
2 *Chemistry of Tin*, ed. P. J. Smith, Springer, Netherlands, Dordrecht, 1998.
3 A. R. W. McKellar, P. R. Bunker, T. J. Sears, K. M. Evenson, R. J. Saykally and S. R. Langhoff, Far infrared laser magnetic resonance of singlet methylene: Singlet–triplet perturbations, singlet–triplet transitions, and the singlet–triplet splittinga, *J. Chem. Phys.*, 1983, **79**, 5251–5264.
4 D. G. Leopold, K. K. Murray, A. E. S. Miller and W. C. Lineberger, Methylene: A study of the X̃ 3B1 and ã 1A1 states by photoelectron spectroscopy of CH−2 and CD−2, *J. Chem. Phys.*, 1985, **83**, 4849–4865.
5 M. E. Colvin, R. S. Grev, H. F. Schaefer and J. Bicerano, X̃ 1A1, ã 3B1, and Ã 1B1 electronic state of silylenes. Structures and vibrational frequencies of SiH2, and SiHF, and SiF2, *Chem. Phys. Lett.*, 1983, **99**, 399–405.
6 J. E. Rice and N. C. Handy, The low-lying states of silylene, *Chem. Phys. Lett.*, 1984, **107**, 365–374.
7 M. S. Gordon, Potential-energy surfaces in singlet and triplet silylene, *Chem. Phys. Lett.*, 1985, **114**, 348–352.
8 K. Balasubramanian and A. D. McLean, The singlet–triplet energy separation in silylene, *J. Chem. Phys.*, 1986, **85**, 5117–5119.
9 M. S. Gordon, D. R. Gano, J. S. Binkley and M. J. Frisch, Thermal decomposition of silane, *J. Am. Chem. Soc.*, 1986, **108**, 2191–2195.
10 S. Koseki and M. S. Gordon, Potential energy surfaces and dynamical properties of three low-lying states of silylene, *J. Mol. Spectrosc.*, 1987, **123**, 392–404.
11 A. Selmani and D. R. Salahub, On the singlet–triplet splitting in SiH2, GeH2, and SnH2. Local-spin-density calculations, *J. Chem. Phys.*, 1988, **89**, 1529–1532.
12 N. Matsunaga, S. Koseki and M. S. Gordon, Relativistic potential energy surfaces of XH2 (X = C, Si, Ge, Sn, and Pb) molecules: Coupling of 1A1 and 3B1 states, *J. Chem. Phys.*, 1996, **104**, 7988–7996.
13 T. Mineva, N. Russo, E. Sicilia and M. Toscano, Spectroscopic constants of SiH2, GeH2, SnH2, and their cations and anions from density functional computations, *Int. J. Quantum Chem.*, 1995, **56**, 669–675.
14 P. P. Gaspar, M. Xiao, D. H. Pae, D. J. Berger, T. Haile, T. Chen, D. Lei, W. R. Winchester and P. Jiang, The quest for triplet ground state silylenes, *J. Organomet. Chem.*, 2002, **646**, 68–79.

15 T. C. Smith and D. J. Clouthier, Detection and characterization of the tin dihydride ($SnH_2$ and $SnD_2$) molecule in the gas phase, *J. Chem. Phys.*, 2018, **148**, 024302.

16 W. P. Neumann, Germylenes and stannylenes, *Chem. Rev.*, 1991, **91**, 311–334.

17 M. Regitz, Stable Carbenes—Illusion or Reality?, *Angew. Chem., Int. Ed. Engl.*, 1991, **30**, 674–676.

18 W. A. Herrmann and C. Köcher, N-Heterocyclic Carbenes, *Angew. Chem., Int. Ed. Engl.*, 1997, **36**, 2162–2187.

19 A. J. I. Arduengo, R. L. Harlow and M. Kline, A stable crystalline carbene, *J. Am. Chem. Soc.*, 1991, **113**, 361–363.

20 D. Bourissou, O. Guerret, F. P. Gabbaï and G. Bertrand, Stable Carbenes, *Chem. Rev.*, 2000, **100**, 39–92.

21 V. Nair, S. Bindu and V. Sreekumar, N-Heterocyclic Carbenes: Reagents, Not Just Ligands!, *Angew. Chem., Int. Ed.*, 2004, **43**, 5130–5135.

22 M. Weidenbruch, Some Silicon, Germanium, Tin, and Lead Analogues of Carbenes, Alkenes, and Dienes, *Eur. J. Inorg. Chem.*, 1999, 373–381.

23 B. Gehrhus and M. F. Lappert, Chemistry of thermally stable bis(amino)silylenes, *J. Organomet. Chem.*, 2001, **617–618**, 209–223.

24 M. Kira, Isolable silylene, disilenes, trisilaallene, and related compounds, *J. Organomet. Chem.*, 2004, **689**, 4475–4488.

25 J. Barrau and G. Rima, Stable germanium analogs of carbenes, imines, ketones, thiones, selones and tellones, *Coord. Chem. Rev.*, 1998, **178–180**, 593–622.

26 P. J. Davidson and M. F. Lappert, Stabilisation of metals in a low co-ordinative environment using the bis(trimethylsilyl)-methyl ligand; coloured Sn II and Pb II alkyls, M[CH-$(SiMe_3)_2]_2$, *J. Chem. Soc., Chem. Commun.*, 1973, 317a.

27 D. H. Harris and M. F. Lappert, Monomeric, volatile bivalent amides of group $IV_B$ elements, $M(NR^1{}_2)_2$ and $M(NR^1R^2)_2$ (M = Ge, Sn, or Pb; $R^1 = Me_3Si$, $R^2 = Me_3C$), *J. Chem. Soc., Chem. Commun.*, 1974, 895–896.

28 A. Togo, F. Oba, I. Tanaka and K. Tatsumi, First-principles calculations of native defects in tin monoxide, *Phys. Rev. B: Condens. Matter Mater. Phys.*, 2006, **74**, 195128.

29 Y. Ogo, H. Hiramatsu, K. Nomura, H. Yanagi, T. Kamiya, M. Kimura, M. Hirano and H. Hosono, Tin monoxide as an s-orbital-based p-type oxide semiconductor: Electronic structures and TFT application, *Phys. Status Solidi A*, 2009, **206**, 2187–2191.

30 *CRC Handbook of Chemistry and Physics*, ed. W. M. Haynes, CRC Press, Boca Raton, 95th edn, 2014.

31 O. R. Gilliam, C. M. Johnson and W. Gordy, Microwave Spectroscopy in the Region from Two to Three Millimeters, *Phys. Rev.*, 1950, **78**, 140–144.

32 A. Hohl, T. Wieder, P. A. van Aken, T. E. Weirich, G. Denninger, M. Vidal, S. Ostwald, C. Deneke, J. Mayer and H. Fuess, An interface clusters mixture model for the structure of amorphous silicon monoxide (SiO), *J. Non-Cryst. Solids*, 2003, **320**, 255–280.

33 J. W. Mellor, *Comprehensive Treatise on Inorganic and Theoretical Chemistry*, John Wiley & Sons, 1972.

34 K. P. Huber and G. Herzberg, *Molecular Spectra and Molecular Structure*, Springer, US, Boston, MA, 1979.

35 *Chemistry of tin*, ed. P. G. Harrison, Blackie & Son, Glasgow, 1989.

36 R. P. Johnson and S. J. W. Price, The Pyrolysis of Tetramethyltin, *Can. J. Chem.*, 1972, **50**, 50–54.

37 S. J. W. Price and A. F. Trotman-Dickenson, Metal-carbon bonds. Part 3.—The pyrolyses of trimethyl bismuth, trimethyl antimony and dimethyl tin dichloride, *Trans. Faraday Soc.*, 1958, **54**, 1630–1637.

38 K. Takahashi, A. Kunz, D. Woiki and P. Roth, Thermal Decomposition of Tin Tetrachloride Based on Cl- and Sn-Concentration Measurements, *J. Phys. Chem. A*, 2000, **104**, 5246–5253.

39 I. S. Zaslonko and V. N. Smirnov, High-temperature reactions of tin atoms with oxygen and nitrous-oxide, *Kinet. Catal.*, 1980, **21**, 602–607.

40 K. Takahashi, A. Giesen and P. Roth, High temperature reaction of $Sn(^3P_0)$ atoms with $O_2$ based on Sn- and O-concentration measurements, *Phys. Chem. Chem. Phys.*, 2001, **3**, 4296–4300.

41 A. Fontijn and P. N. Bajaj, Kinetics of the Sn(3P0) Reactions with CO2 and O2 over Wide Temperature Ranges, *J. Phys. Chem.*, 1996, **100**, 7085–7089.

42 J. R. Wiesenfeld and M. J. Yuen, Kinetic studies of tin and germanium atom oxidation in the gas phase, *J. Phys. Chem.*, 1978, **82**, 1225–1230.

43 M. A. Chowdhury and D. Husain, Kinetic studies of ground state tin atoms, Sn[5p 2(3P 0)], by resonance line absorption, *J. Chem. Soc., Faraday Trans. 2*, 1978, **74**, 1065.

44 P. D. Foo, J. R. Wiesenfeld and D. Husain, Collisional quenching of the spin-orbit states of atomic tin, $Sn(5p^2\ ^3P_2)$ and $Sn(5p^2\ ^3P_1)$, *Chem. Phys. Lett.*, 1975, **32**, 443–448.

45 A. Freedman, R. Behrens, T. P. Parr and R. R. Herm, Crossed molecular beams kinetics: SnO recoil velocity spectra from Sn + O2, *J. Chem. Phys.*, 1978, **68**, 4368–4372.

46 H. Li, S. Pokhrel, M. Schowalter, A. Rosenauer, J. Kiefer and L. Mädler, The gas-phase formation of tin dioxide nanoparticles in single droplet combustion and flame spray pyrolysis, *Combust. Flame*, 2020, **215**, 389–400.

47 R. I. Kaiser, P. Maksyutenko, C. Ennis, F. Zhang, X. Gu, S. P. Krishtal, A. M. Mebel, O. Kostko and M. Ahmed, Untangling the chemical evolution of Titan's atmosphere and surface–from homogeneous to heterogeneous chemistry, *Faraday Discuss.*, 2010, **147**, 429–478.

48 R. I. Kaiser, D. S. N. Parker and A. M. Mebel, Reaction Dynamics in Astrochemistry: Low-Temperature Pathways to Polycyclic Aromatic Hydrocarbons in the Interstellar Medium, *Annu. Rev. Phys. Chem.*, 2015, **66**, 43–67.

49 C. He, Y. Luo, S. Doddipatla, Z. Yang, T. J. Millar, R. Sun and R. I. Kaiser, Gas-phase formation of silicon monoxide via non-adiabatic reaction dynamics and its role as a building block of interstellar silicates, *Phys. Chem. Chem. Phys.*, 2022, **24**, 19761–19772.

50 C. He, S. J. Goettl, Z. Yang, R. I. Kaiser, A. A. Nikolayev, V. N. Azyazov and A. M. Mebel, Gas-Phase Preparation of Subvalent Germanium Monoxide (GeO, $X^1\Sigma^+$) via Non-Adiabatic Reaction Dynamics in the Exit Channel, *J. Phys. Chem. Lett.*, 2022, **13**, 4589–4597.


 

51 Y. Guo, X. Gu, E. Kawamura and R. I. Kaiser, Design of a modular and versatile interlock system for ultrahigh vacuum machines: A crossed molecular beam setup as a case study, *Rev. Sci. Instrum.*, 2006, **77**, 034701.

52 F. G. Kondev, M. Wang, W. J. Huang, S. Naimi and G. Audi, The NUBASE2020 evaluation of nuclear physics properties, *Chin. Phys. C*, 2021, **45**, 030001.

53 N. R. Daly, Scintillation Type Mass Spectrometer Ion Detector, *Rev. Sci. Instrum.*, 1960, **31**, 264–267.

54 M. F. Vernon, PhD dissertation, University of California, 1983.

55 P. S. Weiss, PhD dissertation, University of California, 1986.

56 K. A. Peterson, Systematically convergent basis sets with relativistic pseudopotentials. I. Correlation consistent basis sets for the post-d group 13–15 elements, *J. Chem. Phys.*, 2003, **119**, 11099–11112.

57 B. Metz, H. Stoll and M. Dolg, Small-core multiconfiguration-Dirac–Hartree–Fock-adjusted pseudopotentials for post-d main group elements: Application to PbH and PbO, *J. Chem. Phys.*, 2000, **113**, 2563–2569.

58 D. Giri, R. J. Buenker and K. K. Das, Electronic Spectrum of Tin Oxide: MRDCI Study, *J. Phys. Chem. A*, 2002, **106**, 8790–8797.

59 J.-D. Chai and M. Head-Gordon, Long-range corrected hybrid density functionals with damped atom–atom dispersion corrections, *Phys. Chem. Chem. Phys.*, 2008, **10**, 6615–6620.

60 T. H. Dunning Jr., Gaussian basis sets for use in correlated molecular calculations. I. The atoms boron through neon and hydrogen, *J. Chem. Phys.*, 1989, **90**, 1007–1023.

61 M. J. Frisch, G. W. Trucks, H. B. Schlegel, G. E. Scuseria, M. A. Robb, J. R. Cheeseman, G. Scalmani, V. Barone, B. Mennucci, G. A. Petersson, H. Nakatsuji, M. Caricato, X. Li, H. P. Hratchian, A. F. Izmaylov, J. Bloino, G. Zheng, J. L. Sonnenberg, M. Hada, M. Ehara, K. Toyota, R. Fukuda, J. Hasegawa, M. Ishida, T. Nakajima, Y. Honda, O. Kitao, H. Nakai, T. Vreven, J. A. Montgomery, J. E. Peralta, F. Ogliaro, M. Bearpark, J. J. Heyd, E. Brothers, K. N. Kudin, V. N. Staroverov, R. Kobayashi, J. Normand, K. Raghavachari, A. Rendell, J. C. Burant, S. S. Iyengar, J. Tomasi, M. Cossi, N. Rega, J. M. Millam, M. Klene, J. E. Knox, J. B. Cross, V. Bakken, C. Adamo, J. Jaramillo, R. Gomperts, R. E. Stratmann, O. Yazyev, A. J. Austin, R. Cammi, C. Pomelli, J. W. Ochterski, R. L. Martin, K. Morokuma, V. G. Zakrzewski, G. A. Voth, P. Salvador, J. J. Dannenberg, S. Dapprich, A. D. Daniels, Ö. Farkas, J. B. Foresman, J. V. Ortiz, J. Cioslowski and D. J. Fox, *Gaussian 09 (Revision D.1.)*, Gaussian Inc., Wallingford, CT, 2009.

62 H.-J. Werner, P. J. Knowles, R. Lindh, F. R. Manby, M. Schütz, P. Celani, T. Korona, G. Rauhut, R. D. Amos and A. Bernhardsson, *MOLPRO (Revision 2015.1, A Package of Ab Initio Programs)*, University of Cardiff, Cardiff, UK, 2015.

63 P. Celani and H.-J. Werner, Multireference perturbation theory for large restricted and selected active space reference wave functions, *J. Chem. Phys.*, 2000, **112**, 5546–5557.

64 T. Shiozaki, W. Gyorffy, P. Celani and H.-J. Werner, Communication: Extended multi-state complete active space second-order perturbation theory: Energy and nuclear gradients, *J. Chem. Phys.*, 2011, **135**, 081106.

65 H. Werner and P. J. Knowles, A second order multiconfiguration SCF procedure with optimum convergence, *J. Chem. Phys.*, 1985, **82**, 5053–5063.

66 P. J. Knowles and H.-J. Werner, An efficient second-order MC SCF method for long configuration expansions, *Chem. Phys. Lett.*, 1985, **115**, 259–267.

67 D. Rappoport and F. Furche, Property-optimized Gaussian basis sets for molecular response calculations, *J. Chem. Phys.*, 2010, **133**, 134105.

68 F. Weigend and R. Ahlrichs, Balanced basis sets of split valence, triple zeta valence and quadruple zeta valence quality for H to Rn: Design and assessment of accuracy, *Phys. Chem. Chem. Phys.*, 2005, **7**, 3297–3305.

69 G. D. Purvis and R. J. Bartlett, A full coupled-cluster singles and doubles model: The inclusion of disconnected triples, *J. Chem. Phys.*, 1982, **76**, 1910–1918.

70 R. I. Kaiser, Experimental Investigation on the Formation of Carbon-Bearing Molecules in the Interstellar Medium via Neutral−Neutral Reactions, *Chem. Rev.*, 2002, **102**, 1309–1358.

71 R. I. Kaiser and A. M. Mebel, On the formation of polyacetylenes and cyanopolyacetylenes in Titan's atmosphere and their role in astrobiology, *Chem. Soc. Rev.*, 2012, **41**, 5490.

72 P. Linstrom, *NIST Chemistry WebBook - SRD 69*, National Institute of Standards and Technology, 2023, DOI: **10.18434/T4D303** (Accessed March 2024).

73 R. D. Levine, *Molecular reaction dynamics*, Cambridge University Press, Cambridge, UK, 2005.

74 J. C. Koziar and D. O. Cowan, Photochemical heavy-atom effects, *Acc. Chem. Res.*, 1978, **11**, 334–341.

75 M. Alagia, N. Balucani, L. Cartechini, P. Casavecchia, M. van Beek, G. G. Volpi, L. Bonnet and J. C. Rayez, Crossed beam studies of the O(3P,1D) + CH3I reactions: Direct evidence of intersystem crossing, *Faraday Discuss.*, 1999, **113**, 133–150.

76 D.-Y. Hwang and A. M. Mebel, Ab initio study of spin-forbidden unimolecular decomposition of carbon dioxide, *Chem. Phys.*, 2000, **256**, 169–176.

77 W. D. Geppert, C. Naulin and M. Costes, Integral cross-section of the $C(^3P_j) + O_2(X^3\Sigma_g^-) \rightarrow CO(X^1\Sigma^+) + O(^1D_2)$ reaction between 0.41 and 12.0 kJ $mol^{-1}$, *Chem. Phys. Lett.*, 2002, **364**, 121–126.